Research Article | Open Access

Journal of Materials Informatics

Huang *et al. J. Mater. Inf.* **2026**, *6*, 55 **DOI:**10.20517/jmi.2026.77

Dynamic octahedral freezing and polarization rotation in lead zirconate titanate

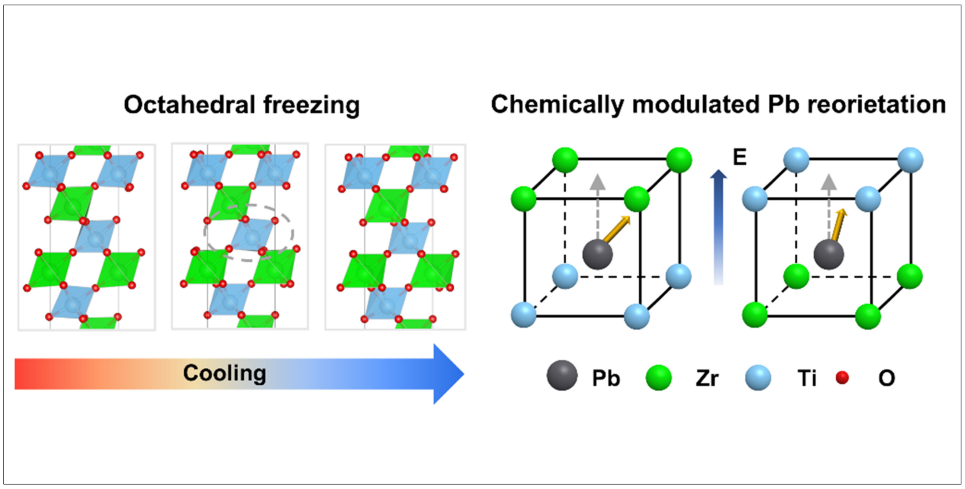
Xiaohan Huang[1], Yihan Nie[2], Haifei Zhan[1,3,*], Gang Zhang[4,5], Chaofeng Lü[1,6,*]

Keywords:
Lead zirconate titanate, machine learning potential, octahedral tilting, morphotropic phase boundary, polarization rotation

Citation: Huang, X.; Nie, Y.; Zhan, H.; Zhang, G.; Lü, C. Dynamic octahedral freezing and polarization rotation in lead zirconate titanate. *J. Mater. Inf.* **2026**, *6*, 55. https://dx.doi.org/10.20517/jmi.2026.77

Received: 27 Aug 2026 **First Decision:** 22 Sep 2026 **Revised:** 21 Oct 2026 **Accepted:** 3 Nov 2026 **Published:** 16 Nov 2026

Academic Editor: Ming Hu
Copy Editor: Pei-Yun Wang
Production Editor: Pei-Yun Wang



Abstract

Lead zirconate titanate (PZT) exhibits outstanding piezoelectric performance, yet its atomistic mechanisms remain ambiguous due to multiscale chemical and structural heterogeneity. Here we employ large-scale molecular dynamics driven by a machine-learning interatomic potential to probe PZT's structural evolution across compositions, temperatures and electric fields. For Zr-rich PZT, the simulations reveal a dynamical crossover within the rhombohedral region, in which local oxygen-octahedral rotational hopping is progressively suppressed upon cooling, leading to effective freezing on the molecular-dynamics timescale. Near the morphotropic phase boundary (MPB), external fields induce polarization rotation through the reorientation of Pb off-center displacements. Local Zr/Ti environments bias the initial displacement orientations and modulate their field-induced reorientation. The trade-off between orientational diversity and greater field-induced reorientability contributes to the superior electromechanical response near the MPB. This work establishes an atomistic link between chemical disorder, local dynamics and composition-dependent piezoelectricity in PZT.

[1]College of Civil Engineering and Architecture, Zhejiang University, Hangzhou 310058, Zhejiang, China.
[2]School of Power and Energy, Northwestern Polytechnical University, Xi'an 710072, Shaanxi, China.
[3]School of Mechanical, Medical and Process Engineering, Queensland University of Technology (QUT), Brisbane QLD 4001, Australia.
[4]School of Materials Science and Engineering, Beijing Institute of Technology, Beijing 100081, China.
[5]School of Aeronautics and Astronautics, Zhejiang University, Hangzhou 310058, Zhejiang, China.
[6]Faculty of Mechanical Engineering & Mechanics, Ningbo University, Ningbo 315211, Zhejiang, China.

***Correspondence to:** Prof. Haifei Zhan, College of Civil Engineering and Architecture, Zhejiang University, Hangzhou 310058, Zhejiang, China. E-mail: zhan_haifei@zju.edu.cn; Prof. Chaofeng Lü, Faculty of Mechanical Engineering & Mechanics, Ningbo University, Ningbo 315211, Zhejiang, China. E-mail: lucf@nbu.edu.cn

INTRODUCTION

Piezoelectric materials, which enable direct interconversion between mechanical and electrical energy, underpin a broad range of electromechanical technologies[1-4]. Despite increasing interest in lead-free piezoelectric materials driven by environmental concerns and emerging applications in wearable electronics and biomedicine[5-8], lead zirconate titanate, $Pb(Zr_{1-x}Ti_x)O_3$ (PZT), remains a benchmark perovskite ferroelectric[9-12]. Its exceptional electromechanical properties are maximized near the morphotropic phase boundary (MPB), where multiple structural instabilities compete.

The conventional description of PZT is based on its composition-dependent phase diagram, in which Ti-rich tetragonal and Zr-rich rhombohedral phases meet near the MPB[13]. This picture was revised by the discovery of monoclinic phases[14-16]. The monoclinic state provides a structural bridge between tetragonal and rhombohedral phases, allowing the polarization direction to rotate between the [001] and [111] directions[17-20]. Monoclinic phase-mediated polarization rotation on a relatively flat free-energy landscape has become a central explanation for the enhanced piezoelectric response of PZT near the MPB[21-25]. Local-structure studies further indicate that Pb displacement directions can deviate from those implied by the average crystallographic symmetry, with their orientational distributions evolving with composition[26]. First-principles studies have linked the preferred directions of Pb off-center displacements to the local Zr/Ti arrangement[27]. How these local chemical environments govern field-induced Pb reorientation and its contribution to the composition-dependent electromechanical response, however, remains insufficiently understood.

The distinction between average symmetry and local structural dynamics is also evident in the Zr-rich region. In the conventional phase diagram, the high-temperature rhombohedral phase, R3m, is commonly described as an average-untilted ferroelectric state, whereas the low-temperature phase, R3c, is distinguished by long-range antiphase oxygen-octahedral tilting[28]. Several experimental studies, however, have suggested that local or disordered octahedral tilting may already exist above the conventional R3m-to-R3c boundary[29-31]. Shi *et al.* also found that weak octahedral tilting persists throughout the simulated rhombohedral region and suggested that thermal broadening of oxygen-position distributions can obscure this tilting in experimental measurements[32]. However, how these local octahedral rotations evolve dynamically upon cooling remains insufficiently understood. Atomistic simulations can bridge local structural dynamics and macroscopic response, but their predictive capability has traditionally been limited by the accuracy and transferability of empirical interatomic potentials[33-37]. Machine learning interatomic potentials offer a way to overcome this limitation by retaining near first-principles accuracy while accessing the length and time scales required to sample finite-temperature dynamics and chemical disorder[32,38-42].

Here, we develop a neuroevolution potential (NEP) for PZT and use large-scale molecular dynamics simulations to resolve its local structural evolution across different compositions, temperatures and electric fields. We show that cooling within the Zr-rich rhombohedral region progressively suppresses local oxygen-octahedral rotational hopping, leading to effective dynamic freezing on the molecular-dynamics timescale. These results provide a dynamical perspective on the evolution of octahedral rotations across the temperature range conventionally associated with the high- and low-temperature rhombohedral states. Near the MPB, external electric fields drive polarization rotation through the reorientation of Pb off-center displacements. The local Zr/Ti environment modulates the initial orientational preferences and field-induced reorientability of these displacements, providing a microscopic perspective on the enhanced electromechanical response. These findings establish an atomistic link between local structural dynamics, chemical disorder and the composition-dependent electromechanical response of PZT.

MATERIALS AND METHODS

Machine learning potential

A machine learning interatomic potential for PZT was developed within the NEP framework[43,44]. The NEP formalism employs radial and angular descriptors to map local atomic configurations to energies and atomic forces, with model parameters optimized using the separable natural evolution strategy (SNES). The overall workflow for constructing the NEP model consists of three main steps, including the construction of the initial training sets, iterative NEP training and active learning to sample structures.

The training dataset was designed to capture structural diversity across the phase space. Representative compositions (x = 0, 0.2, 0.4, 0.5, 0.6, 0.8, 1) were selected, and experimentally reported crystal structures, including cubic, tetragonal, rhombohedral, and monoclinic phases, were incorporated. Based on these reference structures, the configuration space was further expanded by applying various perturbations, including random atomic displacements with magnitudes not exceeding 0.3 Å; volume scaling ranging from 0.90 to 1.10 with an interval of 0.02; and random cell-shape distortions ranging from 0.02 to 0.05 times the cell length with an interval of 0.002. For each individual perturbation and each combination of perturbations, five configurations were generated. In addition, *ab initio* molecular dynamics (AIMD) simulations at x = 0.5 over 0-1,000 K were used to sample four well-converged configurations at each temperature. All structures were labeled using density functional theory (DFT) calculations to obtain their energies, forces and virials. The cutoff radii of the radial and angular descriptors are important hyperparameters for capturing ferroelectric interactions within the finite-range NEP framework. Based on a comparison of prediction errors for different cutoff combinations [Supplementary Table 1], radial and angular cutoff radii of 8 and 6 Å, respectively, were selected.

An iterative active-learning scheme was employed to further refine the potential based on molecular dynamics (MD) simulations. A stepwise heating and cooling scheme was adopted during the MD exploration stage, including 10-300 K, 10-600 K, and 10-1,000 K. All simulations were performed at an external pressure of 0 GPa, while thermal fluctuations naturally sampled a pressure range of approximately -10 to 10 GPa. The effects of different Zr/Ti atomic arrangements were also systematically considered. At each sampling step, ten distinct arrangements were generated for each structure by randomly exchanging Zr and Ti positions while preserving the composition, and each arrangement was used to initiate an MD simulation.

The active-learning procedure was iterated independently for each composition. Candidate configurations were first selected by farthest-point sampling in the descriptor space defined by the NEP model, using a descriptor-distance threshold of 0.01. Configurations were excluded if any atomic force component fell outside the range of -10 to 10 eV/Å or if any interatomic distance was less than 0.7 times the sum of the covalent radii of the corresponding atoms. Among the remaining candidates, configurations with relatively large prediction errors in energies or atomic forces were added to the training set. The iterative procedure was terminated when farthest-point sampling yielded few or no new candidates, or when the remaining candidates exhibited sufficiently small prediction errors in both energies and atomic forces. The final training dataset consists of 2,407 structures and was used to train a unified NEP model.

An independent test set comprising 272 structures was constructed to evaluate the predictive accuracy of the trained NEP model. It included structures generated by atomic displacements along low- and high-frequency phonon modes, perturbed structures with Zr/Ti arrangements different from those in the training set, and structures containing domain walls. These structures were excluded from model training and parameter selection.

DFT calculations

All DFT calculations were performed using the Vienna *ab initio* simulation package (VASP)[45]. The exchange–correlation effects were described using the PBEsol functional, and the projector augmented-wave (PAW) method was employed to describe the core-valence interaction[46,47]. A plane-wave energy cutoff of 600 eV was used. Brillouin zone integrations were performed using Γ-centered k-point meshes with a reciprocal-space resolution of 0.20 $Å^{-1}$. Partial orbital occupancies were determined using the Gaussian smearing method with a width of 0.05 eV. The electronic self-consistency criterion was set to 10^{-8} eV. For structural optimizations, structures were fully relaxed until the magnitude of the residual force on each atom was below 0.01 eV/Å.

Non-spin-polarized AIMD simulations were performed using a 3 × 3 × 3 supercell. Phonon dispersions were calculated using the finite-displacement method implemented in PHONOPY, with a 2 × 2 × 2 supercell used to obtain the force constants[48]. For the cubic phase, non-analytical corrections were included to account for the long-range dipole–dipole interactions responsible for longitudinal optical–transverse optical (LO–TO) splitting.

Atomistic simulations

Large-scale MD simulations were performed using Large-scale Atomic/Molecular Massively Parallel Simulator (LAMMPS) with periodic boundary conditions[49]. All supercell configurations were constructed by replicating standard B-site-centered perovskite primitive cells [Supplementary Figure 1]. The ball-and-stick atomic structure models were generated using Visualization for Electronic and STructural Analysis (VESTA)[50]. The external pressure was fixed at 0.1 GPa. To construct the temperature–composition phase diagram of PZT, a 10 × 10 × 10 supercell (5,000 atoms) was adopted. Compositions ranging from 0 to 1.0 with an interval of 0.02 were sampled. For each composition, the initial structure was chosen as the cubic phase, and quasi-random distributions of Zr and Ti atoms were generated using the Alloy Theoretic Automated Toolkit (ATAT) algorithm[51].

A stepwise cooling protocol was adopted to ensure reliable structural relaxation, with a fixed timestep of 0.5 fs. The temperature was reduced at a rate of 1 K/ps between successive temperature points, followed by an isothermal holding period at each target temperature. The system was cooled from 800 to 650 K and from 300 to 50 K in steps of 50 K, with each temperature held for 50 ps. To enhance the resolution of potential structural transitions in the intermediate regime (600-320 K), a finer temperature interval of 20 K was adopted, accompanied by an extended equilibration period of 100 ps per temperature. Notably, for compositions with x = 0.12-0.56, the cooling sequence from 300 to 50 K was further refined to 25 K intervals, with a holding time of 100 ps at each temperature to investigate structural evolution and rotational dynamics in the rhombohedral region. To assess the sensitivity of local rotational hopping to thermal history and cooling rate, additional simulations were performed at x = 0.40, including heating at 1 K/ps and cooling at 0.5 and 0.2 K/ps.

The polarization-electric field (P-E) hysteresis loops were calculated at 300 K using a 10 × 10 × 10 supercell (5,000 atoms). For each composition, the system was first equilibrated for 40 ps under a negative electric field. Subsequently, a bipolar triangular electric field was applied with a time step of 1 fs and a ramping rate of 1 (kV/cm)/ps. According to previous studies, the rhombohedral phase of $PbZrO_3$ (PZO; x = 0) remains stable below approximately 440 K[40]. Therefore, to allow the emergence of antiferroelectric behavior, simulations for x = 0 were equilibrated at 440 K instead of 300 K.

The field-induced strain behavior was investigated using a 20 × 20 × 20 supercell (40,000 atoms) with a time step of 1 fs. The system was first equilibrated at 300 K for 100 ps, followed by the application of a constant

electric field of 500 kV/cm for 50 ps. After removing the electric field, the system was further equilibrated for 50 ps. To examine the temperature dependence of strain evolution under external electric fields, starting from the equilibrated configuration at 300 K, two additional simulation branches were performed at 200 and 400 K, each equilibrated for 50 ps. Subsequently, an electric field was applied along the z direction, corresponding to the pseudo-cubic $[001]_p$ direction, increasing from 0 to 500 kV/cm in steps of 50 kV/cm, with 20 ps equilibration at each field strength. The longitudinal strain ε_{zz} was extracted to construct strain–electric field (S–E) curves for analyzing piezoelectric strain characteristics. To eliminate uncertainties related to local Zr/Ti ordering, three independent replicas with distinct cation distributions were simulated for each thermodynamic condition.

Since the adopted machine learning potential does not explicitly include long-range electrostatic interactions, external electric fields were incorporated via atom-dependent Born effective charges (BECs). Fixed BEC values were assigned for Pb, Ti, and Zr, namely $Z_{Pb}^{*} = 3.90$, $Z_{Zr}^{*} = 5.85$, $Z_{Ti}^{*} = 7.06$[52]. To enforce charge neutrality, the oxygen BEC was determined from stoichiometry as:

$$Z_{O}^{*} = -\frac{xZ_{Ti}^{*} + (1-x)Z_{Zr}^{*} + Z_{Pb}^{*}}{3} \quad (1)$$

The macroscopic polarization was computed as the total dipole moment of the entire supercell divided by the supercell volume Ω:

$$\boldsymbol{P} = \frac{\sum_i \omega_i Z_i^{*}(\boldsymbol{r}_i - \boldsymbol{r}_{i,cubic})}{\Omega} \quad (2)$$

where ω_i is the lattice-sharing weight accounting for periodic decomposition of the perovskite cell: Pb atoms at the cell vertices carry weight 1/8, oxygen atoms at face centers carry weight 1/2, and B-site cations occupy a full cell with weight 1. $\boldsymbol{r}_i$ and $\boldsymbol{r}_{i,cubic}$ denote the atomic coordinates in the instantaneous low-symmetry structure and the ideal cubic reference structure, respectively. Notably, the polarization vector is calculated for each simulation frame, while Ω is the temperature-averaged volume obtained from fully equilibrated simulation trajectories at the target temperature. The polarization data and cell volume statistics were sampled from identical post-relaxation frames to ensure physical consistency.

Structural analysis

The off-center displacements of A-site Pb cations were evaluated relative to the geometric center of their surrounding oxygen cage, defined by the twelve nearest oxygen neighbors, characterizing the local A-site polar distortion. The off-center displacements of B-site (Zr/Ti) cations were quantified with respect to the center of the corresponding BO_6 oxygen octahedron, defined as the average position of the six coordinating oxygen atoms, providing a measure of B-site local polar distortion. Furthermore, stereographic projections of these cation off-center displacements were plotted with a unified color scale applied to all figures for consistent comparison.

To construct the temperature–composition phase diagram, the lattice parameters and polarization components were averaged over the equilibrated portion of each MD trajectory. The average phase was assigned by combining the lattice metric with the magnitude and orientation of the macroscopic polarization. Cubic, tetragonal and rhombohedral phases were identified from their characteristic lattice symmetries and polarization directions, whereas configurations with two comparable non-zero polarization components and a distinct third component were classified as monoclinic phases. The orthorhombic antiferroelectric region was identified by a negligible net polarization but non-zero spatial averages of the absolute values of two local polarization components. Configurations that did not satisfy any of these symmetry-based criteria were labeled as transition regions. Lattice parameters, cell angles and polarization

components were regarded as equivalent or negligible using tolerances of 0.1 Å, 0.1° and 0.1 C/m², respectively.

For the local-structure analysis at x = 0.42, 0.54 and 0.58, local configurations were classified as T-, R-, O-, M_A-, M_B- or M_C-like based on the orientations of their instantaneous local polarization vectors. Only configurations with local polarization magnitudes ≥ 0.05 C/m² in the analyzed frame at each applied field were included, excluding only 0%-0.025% of the local configurations. To combine symmetry-equivalent domain variants, the absolute vector components were normalized and sorted. The reference directions were $[001]_p$ for T, $[111]_p$ for R and $[011]_p$ for O, while the M_A, M_B and M_C categories corresponded to intermediate orientations along the T–R, R–O and T–O paths, respectively. Each configuration was first assigned to the nearest T, R or O reference direction within an angular tolerance of 15°. The remaining configurations were assigned to the nearest monoclinic path within the same tolerance, using the minimum angular distance to each path. This classification describes local polarization orientations rather than crystallographic phases.

The local rotation of each oxygen octahedron was quantified by aligning instantaneous octahedral configurations with a cubic reference octahedron using the Kabsch optimal rigid-body alignment[53]. For each B-site-centered octahedron, the six surrounding oxygen atoms were translated with respect to the geometric center of the oxygen octahedron, defined as the average position of the six oxygen atoms. The same procedure was applied to the corresponding reference octahedron to ensure a consistent local coordinate definition independent of B-site off-center displacements.

The optimal rotation matrix $\boldsymbol{R}_{k,i}$ was obtained by minimizing the root-mean-square deviation between instantaneous and reference oxygen coordinates after removal of rigid translations, where k denotes the simulation time frame and $\boldsymbol{i} = (i_x, i_y, i_z)$ is the integer index of the unit cell containing the octahedron. The rotation axis $\boldsymbol{n}(k,\boldsymbol{i})$ and rotation angle $\theta(k,\boldsymbol{i})$ were uniquely determined from $\boldsymbol{R}_{k,i}$, and the local rotation vector was defined as:

$$\boldsymbol{\omega}(k,\boldsymbol{i}) = \theta(k,\boldsymbol{i}) \cdot \boldsymbol{n}(k,\boldsymbol{i}) \tag{3}$$

For visualization and statistical analysis, $\boldsymbol{R}_{k,i}$ was further decomposed into extrinsic Euler angles following a sequential X–Y–Z convention, yielding three angular components θ_x, θ_y and θ_z, which represent rotations about the Cartesian axes.

Rotational dynamics analysis

To account for the antiphase nature of octahedral tilts in the perovskite lattice, a staggered transformation was applied to the local rotation vectors, $\boldsymbol{\omega}'(k,\boldsymbol{i}) = \eta_i \cdot \boldsymbol{\omega}(k,\boldsymbol{i})$, where $\eta_i = (-1)^{i_x+i_y+i_z}$. The resulting staggered rotation field was spatially averaged over all octahedra within each simulation frame to obtain the macroscopic rotational vector $\boldsymbol{\Omega}(k)$.

To quantify collective rotational ordering, the spatially averaged staggered rotation vector $\boldsymbol{\Omega}(k)$ was projected onto unit vectors along the eight symmetry-equivalent $\langle 111 \rangle_p$ directions of the pseudo-cubic lattice, and the projection onto each direction was averaged over time. The antiphase tilt order parameter $Q_R^{\langle 111 \rangle}$ was defined as the largest of these eight time-averaged projections. To characterize local rotational states, each local rotation vector was normalized and projected onto the same eight reference vectors. Each octahedron was assigned to the direction yielding the largest projection, and the assignment was accepted only when this maximum projection exceeded 0.8. The rotational time autocorrelation function was computed as:

$$C_\omega(\tau) = \frac{\langle \boldsymbol{\omega}(t_k,\boldsymbol{i}) \cdot \boldsymbol{\omega}(t_k+\tau,\boldsymbol{i}) \rangle}{\langle \boldsymbol{\omega}(t_k,\boldsymbol{i}) \cdot \boldsymbol{\omega}(t_k,\boldsymbol{i}) \rangle} \tag{4}$$

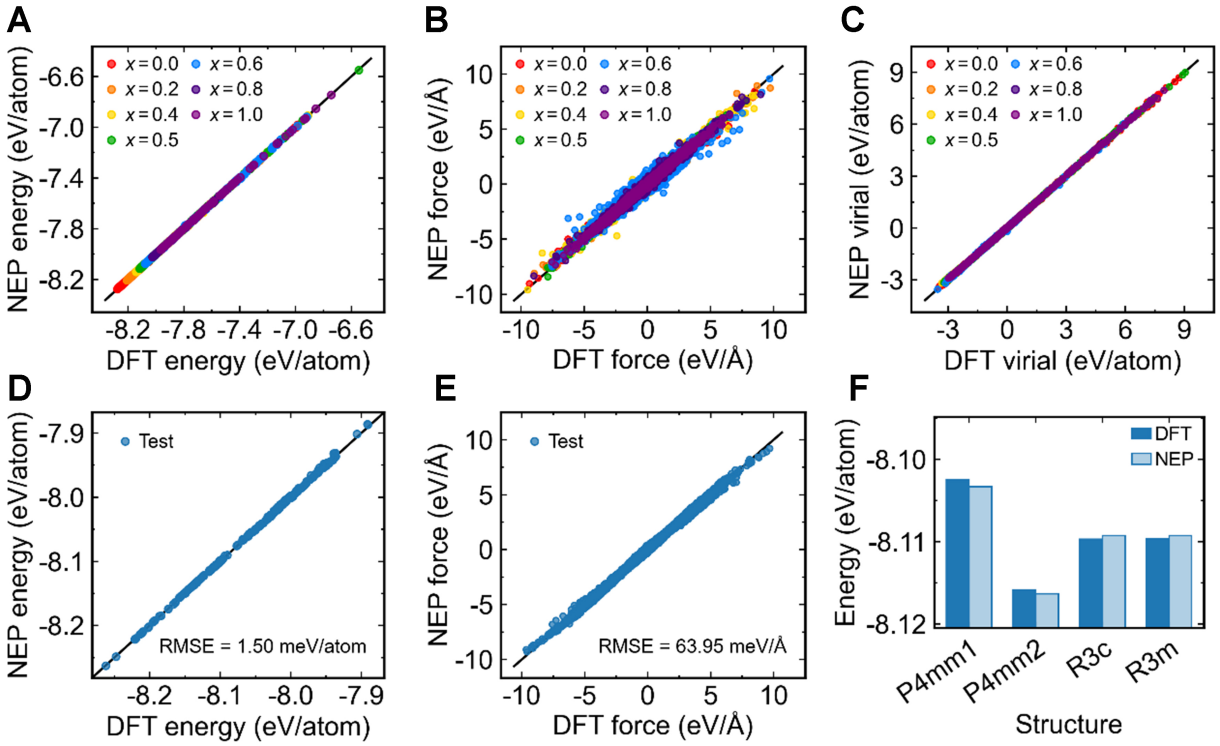


Figure 1. Validation of the NEP against DFT calculations. Comparison between the NEP predictions and DFT reference values for (A) energies per atom, (B) atomic forces and (C) virials per atom in the training set. Colors indicate the Ti fraction *x*. The corresponding root-mean-square errors are 1.63 meV/atom, 76.88 meV/Å and 20.57 meV/atom, respectively; Comparison of NEP predictions with DFT reference values for (D) energies per atom and (E) atomic forces in the independent test set. The corresponding root-mean-square errors are 1.50 meV/atom and 63.95 meV/Å, respectively; (F) Comparison of DFT and NEP energies per atom for four competing structures at *x* = 0.5, labeled P4mm1, P4mm2, R3c and R3m. The corresponding unit-cell structures are shown in Supplementary Figure 2. NEP: Neuroevolution potential; DFT: density functional theory; RMSE: root-mean-square error.

where t_k represents the simulation time ($t_k = k\Delta t$), and τ is the time lag defined as $\tau = (k' - k)\Delta t$, where Δt is the time interval between consecutive saved frames. The brackets denote averaging over all octahedra and all available time origins for each time lag.

For the hopping analysis, a 2-ps moving average was first applied to each Cartesian component of the local rotation vectors to reduce spurious state changes caused by thermal fluctuations. Local rotational states were then assigned using the directional criterion described above. Frames were treated as invalid for a given octahedron if its rotation angle relative to the cubic reference was below 1° or its maximum projection onto the eight reference directions did not exceed 0.8. For each octahedron, invalid frames were skipped, and a hopping event was identified whenever the assigned $<111>_p$ direction differed between consecutive valid frames. The hopping fraction f_{hop} was defined as the fraction of octahedra that exhibited at least one such change during the observation window. The analysis used a 25-ps trajectory window containing 51 frames saved at 0.5-ps intervals.

RESULTS AND DISCUSSION

Validation of the NEP

We first develop a NEP for PZT to enable large-scale finite-temperature molecular dynamics simulations at first-principles accuracy. Figure 1A-C compares the energies, atomic forces and virials predicted by the NEP with the corresponding DFT values for the training set. Across the training configurations, which encompass different compositions, chemical arrangements, structural distortions and thermally perturbed structures, the NEP closely reproduces the DFT data, with root-mean-square errors of 1.63 meV/atom for energy, 76.88 meV/Å for atomic forces and 20.57 meV/atom for atomic virials. These results signify the accuracy of the fitted potential within the configurational space sampled by the training dataset.

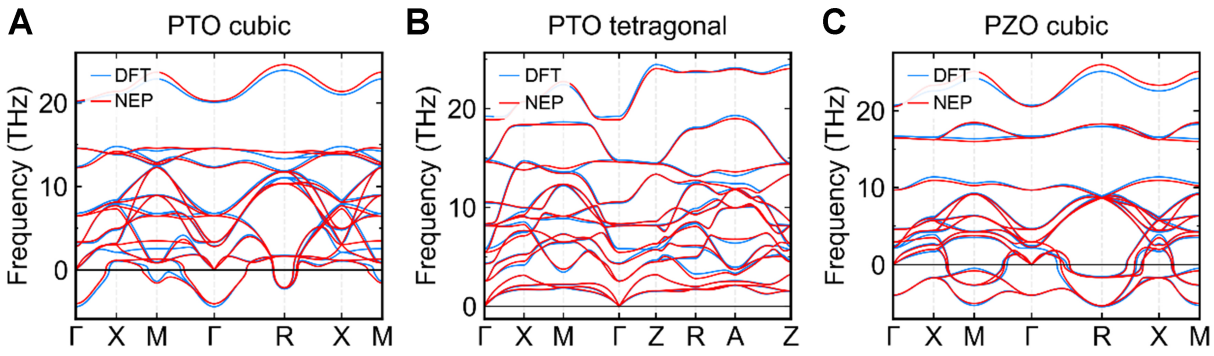


Figure 2. Validation of the NEP lattice dynamics against DFT calculations. (A-C) Phonon dispersions calculated using NEP and DFT for (A) cubic PTO, (B) tetragonal PTO and (C) cubic PZO. NEP: Neuroevolution potential; DFT: density functional theory; PTO: $PbTiO_3$; PZO: $PbZrO_3$.

To assess predictive accuracy beyond the training set, we evaluate the NEP using an independent test set of 272 structures. The predicted energies and atomic forces agree closely with the DFT values, with root-mean-square errors of 1.50 meV/atom and 63.95 meV/Å, respectively [Figure 1D and E]. We further compare the NEP and DFT energies of four competing structures at $x = 0.5$ [Figure 1F], with the corresponding unit-cell structures shown in Supplementary Figure 2. The NEP reproduces the overall energetic ordering. For each structure examined, the absolute deviation between the NEP and DFT energies is below 1 meV/atom. These results support the ability of the NEP to describe the competing structures near the MPB.

We next examine whether the NEP captures the local curvature and structural instabilities of the potential-energy surfaces of the PZT end members. Phonon dispersions are calculated for cubic and tetragonal $PbTiO_3$ (PTO) and cubic PZO, and compared with DFT results. As shown in Figure 2A-C, the NEP reproduces the overall phonon dispersions along the high-symmetry paths, including the imaginary-frequency branches in the cubic phases and the absence of imaginary frequencies along the sampled path in tetragonal PTO. Some deviations remain in individual phonon branches, but the main dispersion features are retained. The agreement indicates that the NEP describes not only the energies and forces of individual configurations, but also the local potential-energy-surface curvature underlying the lattice dynamics of these end-member structures.

We then assess the transferability of the NEP to finite-temperature structural evolution across the full PZT composition range. Large-scale molecular dynamics simulations are performed at 300 K for compositions from $x = 0$ to 1 in increments of 0.02. The spontaneous polarization vectors (**P**) and local oxygen-octahedral rotation angles (θ_x, θ_y, θ_z) are defined relative to the corresponding high-temperature cubic reference structures, as illustrated in Figure 3 and detailed in Methods. With increasing Ti content, the calculated polarization and octahedral-rotation characteristics exhibit a systematic compositional evolution [Figure 4A and B], recovering the established room-temperature sequence from the Zr-rich antiferroelectric orthorhombic state, through the ferroelectric rhombohedral region, to the Ti-rich ferroelectric tetragonal state[13]. The emergence of these distinct structures from finite-temperature simulations demonstrates that the NEP captures the competition among antipolar displacements, ferroelectric distortions and oxygen-octahedral rotations across chemically disordered compositions.

The response to an external electric field provides a further test of the model beyond equilibrium structural properties. Figure 4C and D shows P-E hysteresis loops calculated at 300 K for the Ti-containing compositions and at 440 K for $x = 0$. The $x = 0$ composition displays a double hysteresis loop characteristic of

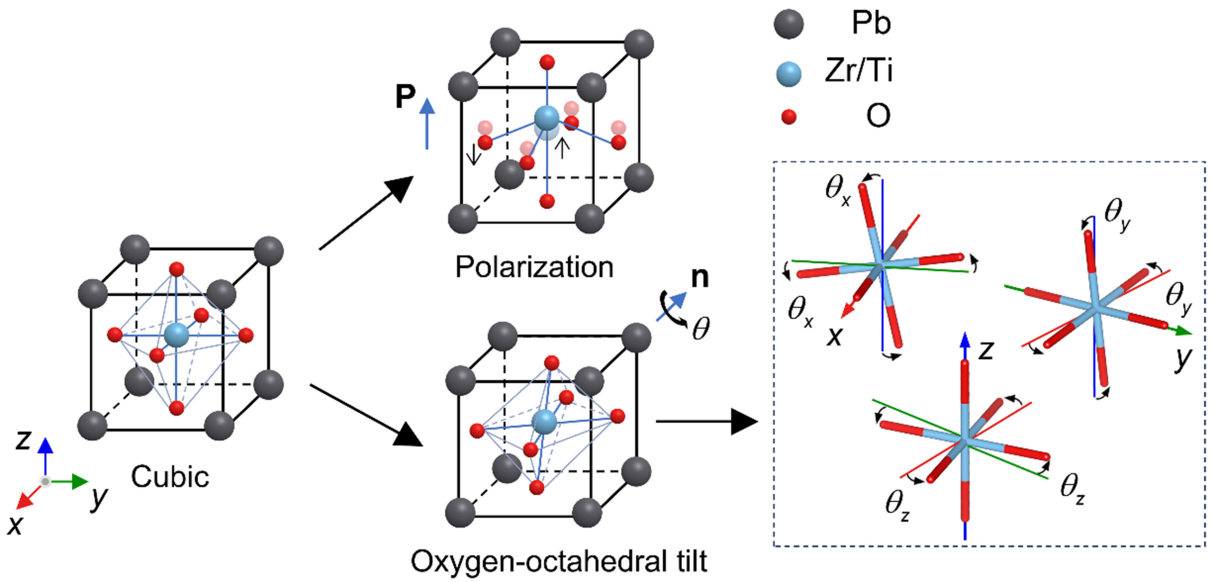


Figure 3. Schematic illustration of the perovskite unit cell and its local structural descriptors. The spontaneous polarization vector and oxygen-octahedral rotation angles are indicated. The atomic structures in the octahedral-rotation diagrams were visualized using VESTA[50]. VESTA: Visualization for Electronic and STructural Analysis.

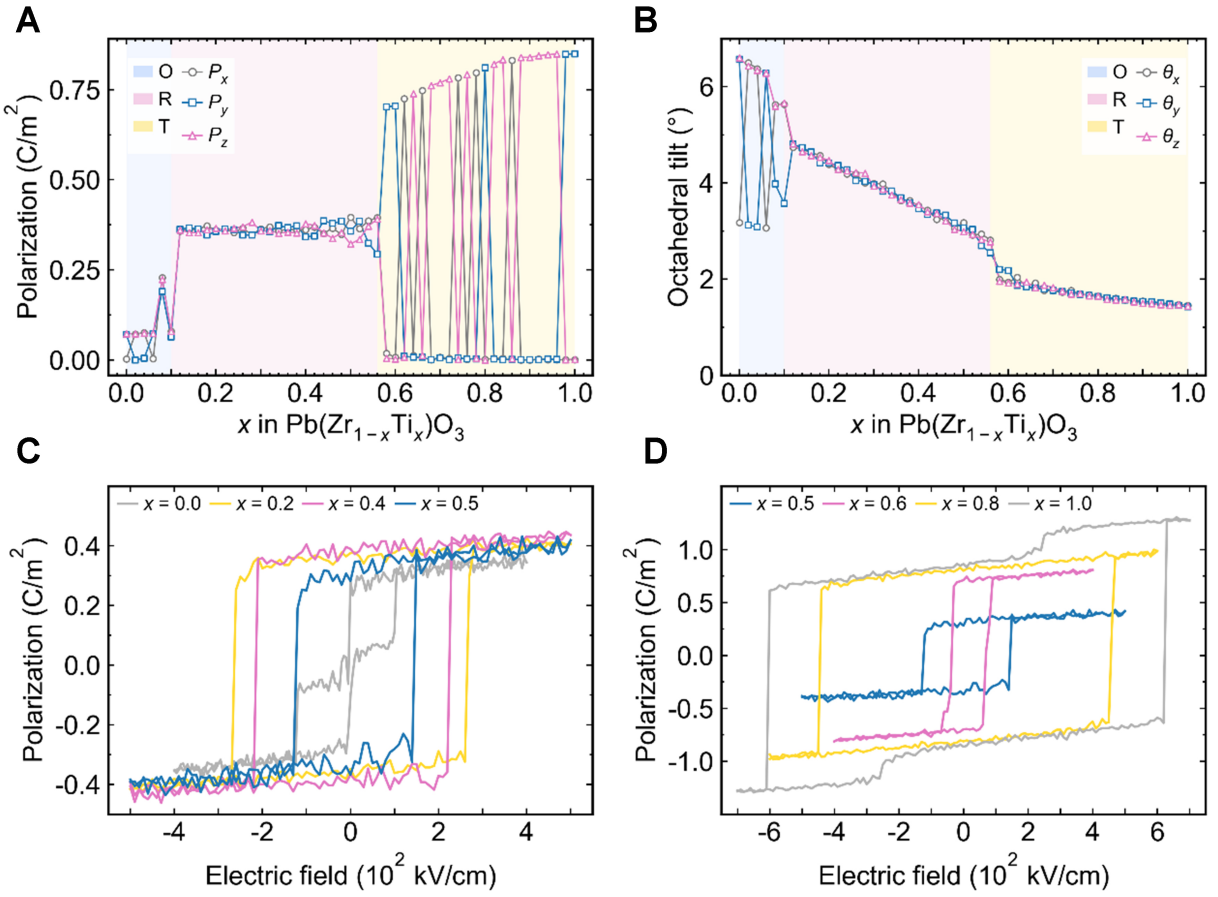


Figure 4. Composition-dependent structural characteristics, spontaneous polarization and P-E hysteresis loops of PZT. (A) Components of the spontaneous polarization along the three Cartesian axes at 300 K; (B) Oxygen-octahedral rotation angles about the three Cartesian axes at 300 K. O, R and T represent the orthorhombic, rhombohedral and tetragonal phases, respectively; (C and D) P-E hysteresis loops of PZT with different compositions at 300 K, shown for the composition ranges of (C) x = 0-0.5, and (D) x = 0.5-1.0. All hysteresis loops were calculated at 300 K, except for x = 0 (PZO), which was calculated at 440 K. P-E: Polarization-electric field; PZT: lead zirconate titanate; PZO: $PbZrO_3$.

antiferroelectric switching, while the Ti-containing compositions display single ferroelectric loops. Compositions near the MPB exhibit comparatively low coercive fields, indicating that their polarization configurations can be reorganized more readily under an applied field. The decrease in coercive field from the Ti-rich side towards the MPB is qualitatively consistent with the experimental trend reported by Gerber *et al.* for PZT thin films[54]. The high-field polarization increases with Ti content in the tetragonal region, consistent with the composition dependence of polarization reported by Morioka *et al.* for polar-axis-oriented tetragonal PZT films[55]. These comparisons support the simulated compositional trends, although the experimental films and the present simulations differ in microstructure, boundary conditions and field-sweep timescale.

Together, the agreement with DFT reference data for training and independent test configurations, the reproduction of phonon dispersions, and the recovery of composition-dependent structural and switching behavior support the accuracy and transferability of the NEP. These results provide a basis for investigating the local octahedral-rotation dynamics, field-driven polarization rotation and effects of local chemical environments discussed below.

Dynamic freezing of octahedral rotations in Zr-rich PZT

We next use the NEP to investigate octahedral ordering and rotational dynamics upon cooling in Zr-rich PZT, with reference to the conventional R3m–R3c phase boundary. At the average-structure level, R3m and R3c are distinguished by the absence or presence, respectively, of long-range antiphase oxygen-octahedral tilting about a $<111>_p$ axis[28]. For the structures examined at $x = 0.4$, the NEP reproduces the DFT energetic preference for R3c over R3m, although it overestimates their energy separation [Supplementary Figure 3]. To investigate the finite-temperature evolution of octahedral rotations, we determine the local rotation vector $\boldsymbol{\omega}(k,\boldsymbol{i})$ of each oxygen octahedron ($\boldsymbol{i}$) in each simulation frame (k), relative to the corresponding high-temperature cubic structure. Here, rotation refers to the rigid-body rotation of an individual octahedron, whereas tilt denotes the collective mode formed by spatially correlated octahedral rotations.

For each frame, the local rotation vectors are multiplied by the antiphase factors $\eta(\boldsymbol{i})$, yielding the staggered rotation vectors $\boldsymbol{\omega}'(k,\boldsymbol{i})$. These vectors are spatially averaged to obtain $\boldsymbol{\Omega}(k)$, which is then projected onto unit vectors along the eight symmetry-equivalent $<111>_p$ directions. The projection along each direction is averaged over time, and the largest of these time-averaged projections defines the antiphase tilt order parameter $Q_R^{<111>}$. To reveal the local origin of this collective response, we also calculate the distribution of local rotation directions by pooling the assigned $<111>_p$ states over all octahedra and sampled frames at each temperature.

The results in Figure 5A and B reveal three regimes of the octahedral-rotation behavior. At high temperatures, $Q_R^{<111>}$ remains close to zero, while the local rotation vectors in $Pb(Zr_{0.6}Ti_{0.4})O_3$ are broadly distributed among several symmetry-equivalent $<111>_p$ directions. A representative local trajectory, smoothed using a 2-ps moving average, shows nonzero, time-dependent rotation components at high temperatures [Supplementary Figure 4]. Together, these observations indicate that the near-zero order parameter does not imply the absence of local rotations, but instead indicates little collective antiphase order after spatial and temporal averaging. Upon cooling, $Q_R^{<111>}$ increases rapidly across the narrow temperature interval marked by densely spaced contours. Concurrently, the local rotation-direction distribution becomes concentrated along a pair of opposite $<111>_p$ directions. These directions define a common crystallographic axis; their predominance, together with the increase in $Q_R^{<111>}$, indicates collective tilt-axis selection accompanied by the development of antiphase order. Below this narrow axis-selection interval, $Q_R^{<111>}$ continues to increase more gradually over a broad temperature range, while the same tilt axis remains

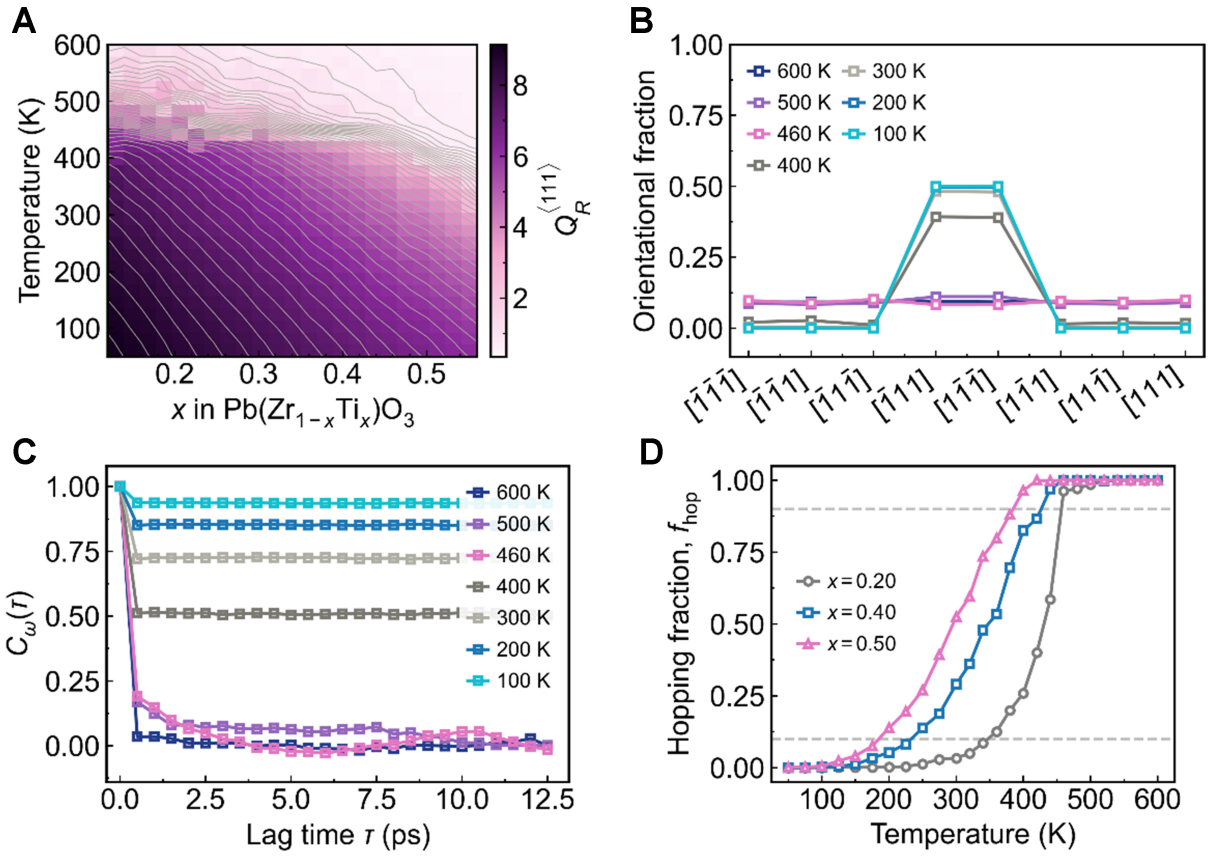


Figure 5. Collective antiphase ordering and local rotational dynamics of oxygen octahedra in PZT. (A) Composition and temperature dependence of the antiphase octahedral-tilt order parameter $Q_R^{\langle 111\rangle}$. Grey contour lines are drawn at intervals of 0.2; (B) Distribution of local oxygen-octahedral rotation directions in $Pb(Zr_{0.6}Ti_{0.4})O_3$ at selected temperatures. Each fraction represents the population assigned to the corresponding $\langle 111\rangle_p$ direction, pooled over all octahedra and sampled frames without first averaging the rotation vectors over time; (C) Time autocorrelation functions $C_\omega(\tau)$ of the local rotation vectors in $Pb(Zr_{0.6}Ti_{0.4})O_3$ at different temperatures; (D) Temperature dependence of the octahedral-rotation hopping fraction f_{hop} for x = 0.20, 0.40 and 0.50. Horizontal dashed lines indicate the thresholds of 0.9 and 0.1 used to define T_{R1} and T_{R2}, respectively. PZT: Lead zirconate titanate.

dominant, indicating a further increase in the collective antiphase rotation amplitude along the selected axis. The axis-selection temperature shifts systematically to lower values with increasing Ti content.

The structural quantities alone do not determine whether the local rotations remain dynamically active after the collective tilt axis has been selected. We therefore calculate the time autocorrelation function $C_\omega(\tau)$ of the local rotation vectors in $Pb(Zr_{0.6}Ti_{0.4})O_3$, together with the octahedral-rotation hopping fraction f_{hop} [Figure 5C and D]. Here, f_{hop} is defined as the fraction of octahedra whose assigned local $\langle 111\rangle_p$ rotation state changes at least once during the 25-ps observation window, using the filtering criteria described in the Methods. For x = 0.4, at high temperatures (460-600 K), $C_\omega(\tau)$ decays rapidly to approximately zero and f_{hop} remains close to unity, indicating that nearly all octahedra explore multiple rotation states during the sampled trajectory. At intermediate temperatures (300-400 K), $C_\omega(\tau)$ develops a finite plateau over the sampled lag times and f_{hop} decreases progressively. Together with the orientational distributions, these results indicate that a preferred collective tilt axis coexists with ongoing local rotational hopping. Analysis of the angular separation between successive valid $\langle 111\rangle_p$ states shows that rotational hopping predominantly occurs between neighboring directions separated by approximately 71°. Hopping events between directions separated by approximately 109° become more frequent at higher temperatures, whereas 180° reversals remain rare [Supplementary Figure 5]. With further cooling (100-200 K), $C_\omega(\tau)$ shows only a small initial decay followed by a high plateau, and f_{hop} approaches zero, indicating that the local rotation states become

effectively frozen within the sampled observation window. Similar temperature-dependent suppression of rotational hopping is observed for x = 0.20 and 0.50, although the characteristic temperatures differ among compositions [Figure 5D].

To characterize this progressive suppression, we define two characteristic temperatures as T_{R1} and T_{R2}. Specifically, T_{R1} is the temperature at which f_{hop} first falls below 0.9 upon cooling, marking the onset of suppression of rotation-state hopping. T_{R2} is the temperature at which f_{hop} first falls below 0.1, marking the approach to dynamic freezing within the finite simulation window. These temperatures serve as operational markers of the dynamical crossover rather than independently determined thermodynamic phase boundaries. Varying the upper threshold from 0.85 to 0.95 and the lower threshold from 0.05 to 0.15 shifts the extracted temperatures but preserves their overall compositional trends [Supplementary Figure 6]. For the composition tested, heating and cooling at 1 K/ps and cooling at reduced rates of 0.5 and 0.2 K/ps yield closely overlapping hopping-fraction curves, indicating weak sensitivity to the heating/cooling direction and cooling rate within the tested range [Supplementary Figure 7A]. Other Zr-rich compositions exhibit a similar evolution from an orientationally disordered multistate regime, through an axis-selected fluctuating regime, to a dynamically frozen state [Supplementary Figure 7B]. Both characteristic temperatures generally shift to lower values with increasing Ti content.

To place the dynamical evolution in the context of the conventional phase behavior, we construct the temperature–composition phase diagram from the average lattice parameters and polarization and superimpose the calculated T_{R1} and T_{R2} values [Figure 6]. For x = 0.12-0.40, T_{R1} (dark-blue line) closely tracks the paraelectric–rhombohedral boundary. Together with the structural analysis above, this correspondence suggests that collective tilt-axis selection and the onset of suppression of rotational hopping occur on a similar temperature scale to the emergence of the rhombohedral state. Within this composition range, the antiphase tilt order parameter remains clearly nonzero below T_{R1}, indicating that no separate average-untilted R3m regime is resolved. T_{R2} (light-blue line) lies well within the rhombohedral region. The interval between T_{R1} and T_{R2} consequently characterizes a dynamical crossover during which a preferred collective tilt axis is maintained while local rotational hopping, predominantly between neighboring $<111>_{\mathrm{p}}$ directions separated by approximately 71°, is progressively suppressed on cooling.

The absence of a distinct R3m region in simulations contrasts with the conventional experimental phase diagram. One possible explanation, suggested by Shi *et al.*, is that weak tilt-related diffraction signals may be difficult to resolve experimentally[32], although this possibility is not directly tested here. We also compare T_{R2} with the experimental R3m–R3c boundary to examine the relationship between structural ordering and the suppression of local rotational hopping. Here, T_{R2} is a dynamical marker, not a simulated structural phase boundary. The calculated T_{R2} values lie below the experimentally reported boundary. This difference may partly reflect the distinct criteria used: T_{R2} represents near-complete suppression of local rotation-state hopping within a 25-ps observation window, whereas the experimental boundary is identified from diffraction signatures of structural ordering, including superlattice reflections associated with antiphase octahedral tilting. Because structural ordering does not necessarily require local rotational hopping to cease, a diffraction-based R3c assignment may occur above T_{R2}.

The simulated paraelectric-to-low-symmetry boundary lies below its experimental counterpart. Underestimated ferroelectric transition temperatures have also been reported in PBEsol-based simulations of $BaTiO_3$ and PTO[56,57], indicating that limitations of the reference exchange–correlation functional may contribute to the discrepancy observed here. Paul *et al.* showed that incorporating anharmonic coupling between soft polar modes and higher-energy phonon modes improves underestimated transition temperatures in effective-Hamiltonian simulations[58]. Although the present all-atom NEP simulations retain

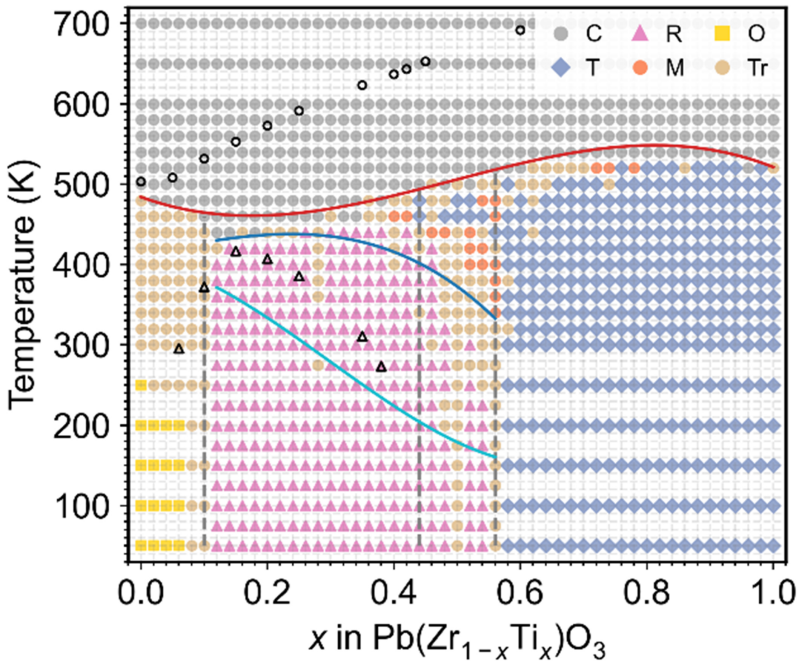


Figure 6. Temperature–composition phase diagram of PZT predicted by the NEP. The phase at each temperature and composition is assigned from the lattice parameters and macroscopic polarization averaged over the equilibrated MD trajectories, with different colors denoting distinct average structural symmetries or transition regions. The phase labels correspond to cubic (C), tetragonal (T), rhombohedral (R), orthorhombic (O), monoclinic (M), and transition regions (Tr). Three vertical black dashed lines divide the phase diagram into four composition regions: orthorhombic, rhombohedral, MPB and tetragonal regions with increasing Ti content. The dark-blue line and light-blue line mark the characteristic temperatures T_{R1} and T_{R2}, respectively. Open black diamonds denote the experimentally reported R3m–R3c boundary[13]. The red line marks the simulated transition temperature between the paraelectric cubic phase and the low-symmetry phases, and open black squares denote the corresponding experimental transition temperatures[13]. PZT: Lead zirconate titanate; NEP: neuroevolution potential; MD: molecular dynamics; MPB: morphotropic phase boundary.

these degrees of freedom, the accuracy of the relevant anharmonic couplings has not been separately assessed; the overall fitting errors and phonon benchmarks alone do not establish this accuracy. Finite-size effects provide another possible contribution, as demonstrated for $BaTiO_3$ by Gigli *et al.*[59]. However, convergence with production-cell size must be distinguished from the transferability of the potential: Li *et al.* found that short-range models trained on small cells can lose accuracy when applied to larger cells. Their study also showed that including explicit long-range electrostatics improves agreement with reference DFT forces but lowers the predicted Curie temperature of PTO, illustrating that closer agreement with experiment can result from error cancellation[57]. The relative contributions of these factors have not been quantified in the present work. Future work will investigate qNEP[60] with explicit long-range electrostatics, alongside systematic tests of training-cell and production-cell sizes, to assess their effects on the predicted transition temperatures.

Electric-field-driven polarization rotation near the MPB

We next investigate the microscopic origin of the enhanced electromechanical response near the MPB by applying an electric field along $[001]_p$. At all three temperatures, the field-induced longitudinal strain is largest near the MPB and substantially smaller in the Zr-rich and Ti-rich regions [Figure 7A-C], qualitatively consistent with the enhanced macroscopic piezoelectric response of PZT near the MPB.

To determine how the local structure evolves under the field, we track the fractions of R-, O-, M_A-, M_B-, M_C- and T-like local polar configurations, classified according to their instantaneous local polarization directions, for representative Zr-rich (x = 0.42), MPB (x = 0.54) and Ti-rich (x = 0.58) compositions [Figure 7D-F]. At

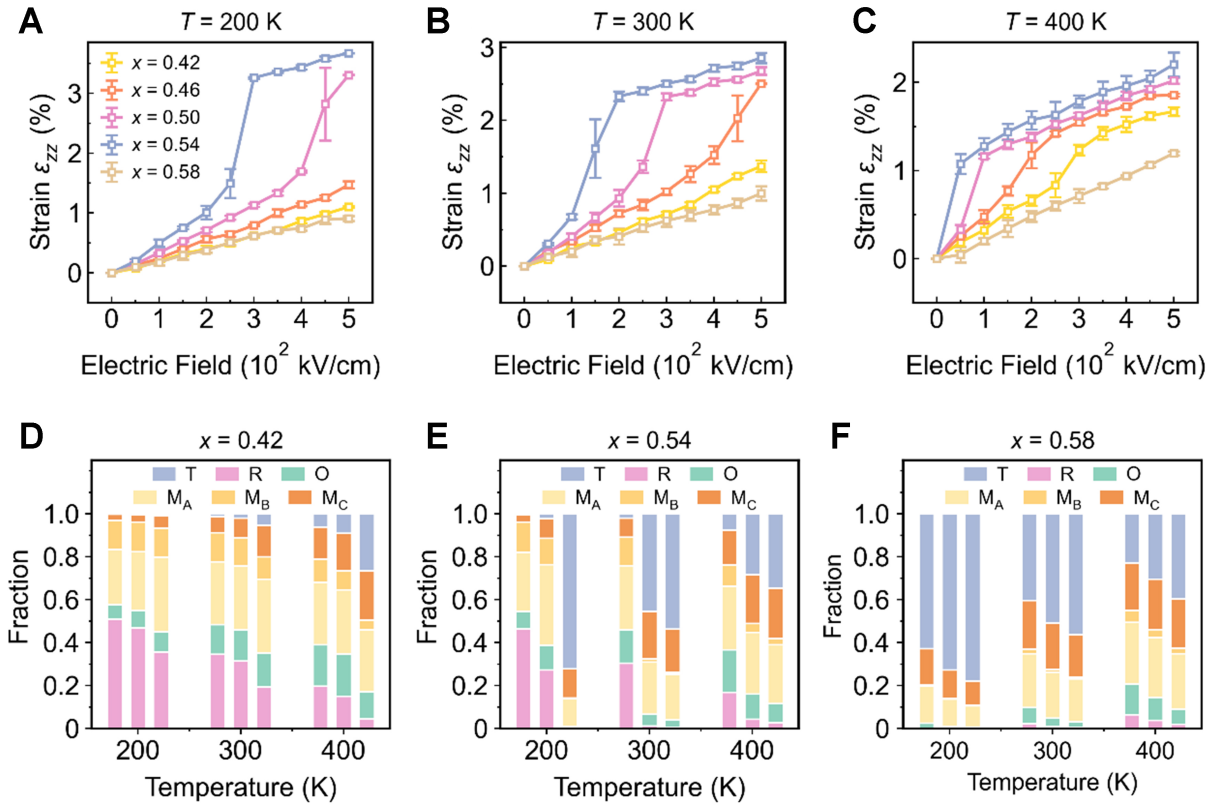


Figure 7. Electric-field-induced strain response and evolution of local polar configurations in PZT. (A-C) Electric-field dependence of the longitudinal strain ε_{zz} for different PZT compositions under an electric field applied along the z direction ($[001]_p$) at (A) 200 K, (B) 300 K and (C) 400 K. The color–composition mapping is defined in panel (A); lines in panels (B) and (C) follow the same color scheme. All strain data are extracted from the final equilibrated snapshots after structural relaxation at each electric field. Error bars represent the standard deviation computed from three independent simulation replicas; (D-F) Fractions of local polar configurations classified as T-, R-, O-, M_A-, M_B- and M_C-like according to their instantaneous local polarization directions for (D) x = 0.42, (E) x = 0.54 and (F) x = 0.58. The classification uses an angular tolerance of 15° and assigns each classified configuration to a single category (Methods). These labels describe local polarization orientations rather than crystallographically identified phases. At each temperature, the three bars correspond, from left to right, to electric fields of 0, 200 and 400 kV/cm. PZT: Lead zirconate titanate.

zero field, both x = 0.42 and x = 0.54 exhibit substantial monoclinic-like populations, defined here as the combined M_A-, M_B- and M_C-like fractions. Their responses to the applied field, however, differ markedly. For x = 0.54, the T-like fraction increases strongly with field at all three temperatures, whereas the increase is much smaller for x = 0.42. At zero field, the x = 0.58 composition contains a substantial T-like population and a smaller monoclinic-like fraction. Its field-induced strain response is also weaker than that of x = 0.54. Taken together, these comparisons indicate that the initial monoclinic-like population alone cannot account for the enhanced electromechanical response near the MPB.

To examine the field-induced orientational changes more directly, we analyze the distributions of instantaneous local Pb off-center displacement directions [Figure 8], together with the angle between the spatially averaged Pb displacement vector and the applied field [Figure 9]. Both quantities are evaluated from the final equilibrated frame at each field strength. The orientational distributions are estimated on the unit sphere using spherical kernel density estimation and displayed by stereographic projection, with color representing probability density per unit solid angle.

At 300 K, the zero-field distributions of both compositions are centered near $[111]_p$ and extend into intermediate orientational regions. Increasing the field along $[001]_p$ produces a relatively modest shift for x = 0.42, whereas the distribution for x = 0.54 shifts markedly towards $[001]_p$ and becomes concentrated near this

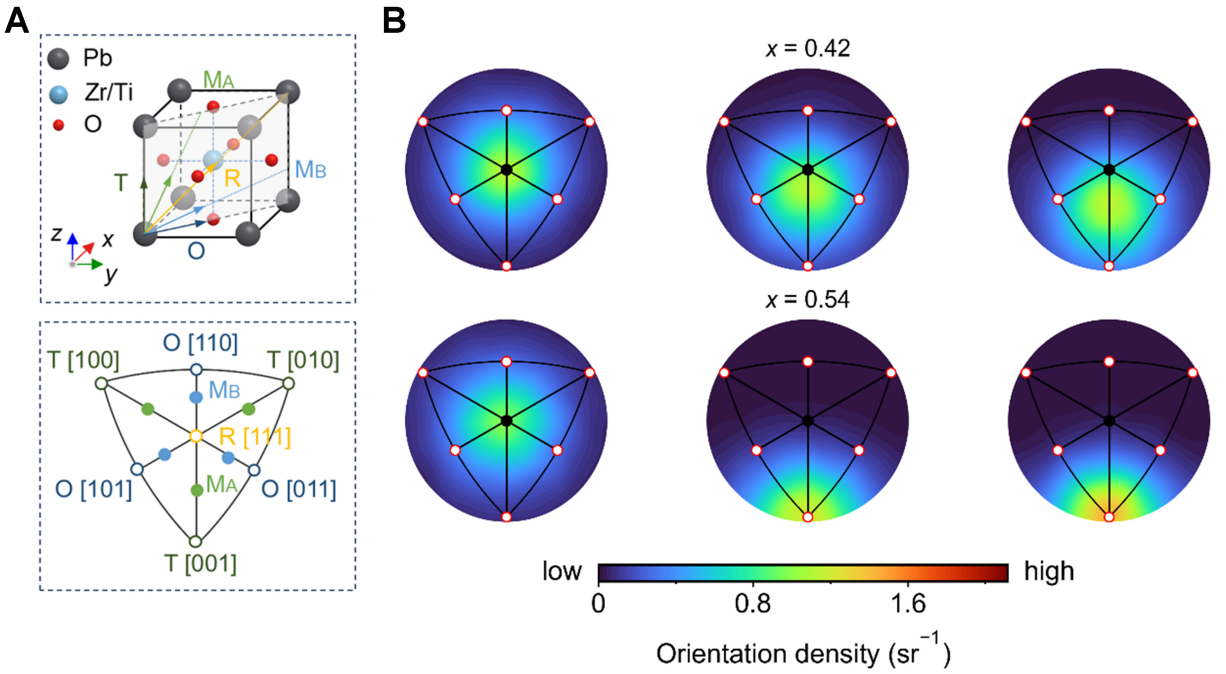


Figure 8. Evolution of Pb off-center displacement directions under an applied electric field. (A) Top, schematic illustration of Pb off-center displacement vectors within the $(1\bar{1}0)_p$ plane, showing characteristic T-like ($[001]_p$), R-like ($[111]_p$), O-like ($[110]_p$), M_A-like (between R and T) and M_B-like (between R and O) orientations. Bottom, stereographic representation of these orientations and their symmetry-equivalent directions, viewed along $[111]_p$. These labels denote displacement orientations rather than crystallographically identified phases; (B) Orientational probability density maps of the instantaneous Pb off-center displacement vectors for x = 0.42 (top row), and x = 0.54 (bottom row) at 300 K. Columns correspond to electric fields of 0, 100 and 300 kV/cm, applied along $[001]_p$. Each distribution includes all Pb sites in the final equilibrated frame at the corresponding field strength, without temporal averaging. Probability densities are estimated on the unit sphere using spherical kernel density estimation and displayed by stereographic projection. Colors represent probability density per unit solid angle (sr^{-1}), rather than per unit projected area.

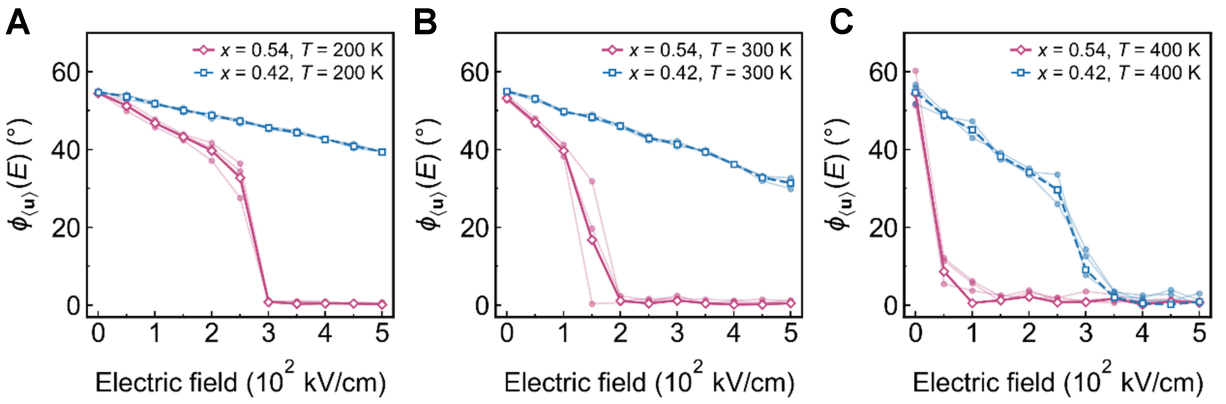


Figure 9. Electric-field dependence of the mean Pb displacement orientation. (A-C) Angle $\phi_{\langle u \rangle}(E)$ between the spatially averaged Pb off-center displacement vector and the applied-field direction, $[001]_p$, for x = 0.42 and x = 0.54 at (A) 200 K, (B) 300 K and (C) 400 K. At each field strength, the displacement vectors are averaged over all Pb sites in the final equilibrated frame before the angle is calculated. No temporal averaging is performed. Light-colored lines with circular markers show the angles obtained from three independent simulation replicas; dark-colored lines with square or diamond markers show the mean of these angles across the replicas. A value approaching zero indicates alignment of the mean displacement with the field.

direction at 300 kV/cm [Figure 8B]. The redistribution through the M_A-like orientational region is consistent with a collective polarization-rotation tendency along the R → M_A → T pathway. The distributions at 200 and 400 K likewise show that x = 0.54 develops field-directed orientations more readily than x = 0.42 [Supplementary Figures 8 and 9].

The spatially averaged displacement angle quantifies this contrast [Figure 9]. At 200 and 300 K, the mean Pb displacement in $x = 0.54$ approaches alignment with the field at approximately 300 and 200 kV/cm, respectively, whereas $x = 0.42$ retains a substantial angular deviation at 500 kV/cm. At 400 K, both compositions approach alignment, with $x = 0.54$ requiring a considerably lower field. The pronounced angular decreases occur over field intervals that also exhibit strong increases in longitudinal strain [Figure 7A-C], supporting a connection between polarization rotation and the enhanced electromechanical response.

To examine the corresponding response at individual sites, we follow the time-averaged, symmetry-folded displacement vectors of one selected Pb atom from each of three independent simulation replicas for each composition at 300 K [Supplementary Figures 10 and 11]. The averaging and symmetry-folding procedure is specified in the supplementary figure captions. All three selected sites in $x = 0.54$ show an overall rotation of their mean displacement directions towards the applied field, whereas the selected sites in $x = 0.42$ exhibit more varied responses, with some retaining substantial displacement components perpendicular to the field. Nonmonotonic changes and finite displacement components normal to the plane containing $[111]_p$ and $[001]_p$ show that individual-site responses can depart from the ideal R → M_A → T route. These field-dependent mean configurations illustrate local rotation without establishing a smooth, continuous microscopic trajectory.

Ti and Zr displacement distributions also shift towards $[001]_p$ at 300 K, particularly for $x = 0.54$, indicating that multiple cations participate in the orientational response [Supplementary Figures 12 and 13].

Together, these observations indicate that a substantial initial monoclinic-like population alone is insufficient to explain the enhanced response near the MPB. Instead, the results support a polarization-rotation mechanism in which local displacement orientations in $x = 0.54$ are more readily redirected from R-like towards T-like orientations under the applied field, accompanying its larger longitudinal strain.

Local chemical control of Pb-displacement reorientation

The contrasting field-induced orientational responses of $x = 0.42$ and $x = 0.54$ motivate an examination of how the local chemical environment influences Pb-displacement reorientation. Motivated by the stronger Zr-Pb repulsion relative to Ti-Pb interactions reported previously[27], we classify each Pb site according to the Zr content of the two pseudo-cubic $(001)_p$ planes formed by its eight nearest Zr/Ti neighbors. A plane containing at least three Zr atoms is classified as Zr-rich. Zr-up and Zr-down denote environments containing a single Zr-rich plane above or below the Pb atom, respectively; Zr-Zr denotes environments in which both planes are Zr-rich; and other-environments comprise the remaining configurations. Above and below refer to the positive and negative z directions, respectively, with the electric field applied along $[001]_p$. A representative Zr-up configuration is shown in Supplementary Figure 14.

To examine the corresponding local energetics within the NEP, we perform constrained Pb-displacement rotation scans for selected sites in an energy-minimized configuration of $x = 0.40$, obtained from a zero-field trajectory at 300 K [Supplementary Figure 15]. For these illustrative scans, each neighboring plane consists entirely of Zr or Ti, providing chemically distinct examples of Zr-Zr, Zr-down, Zr-up and Ti-Ti environments. Each Pb displacement is rotated at fixed magnitude within the plane spanned by its initial direction and $[001]_p$, while all other atoms and the simulation cell remain fixed. The selected Zr-down site has the smallest initial deviation from $[001]_p$, whereas the Zr-up site has the largest. The Zr-down energy profile also shows a greater energy cost for rotation away from $[001]_p$ than towards it, whereas the Zr-Zr profile is approximately symmetric over the sampled angular range. Taken together, the initial orientational biases and the contrasting asymmetries of the rotation-energy profiles provide qualitative support for a tendency of Pb displacements to avoid Zr-rich neighboring planes.

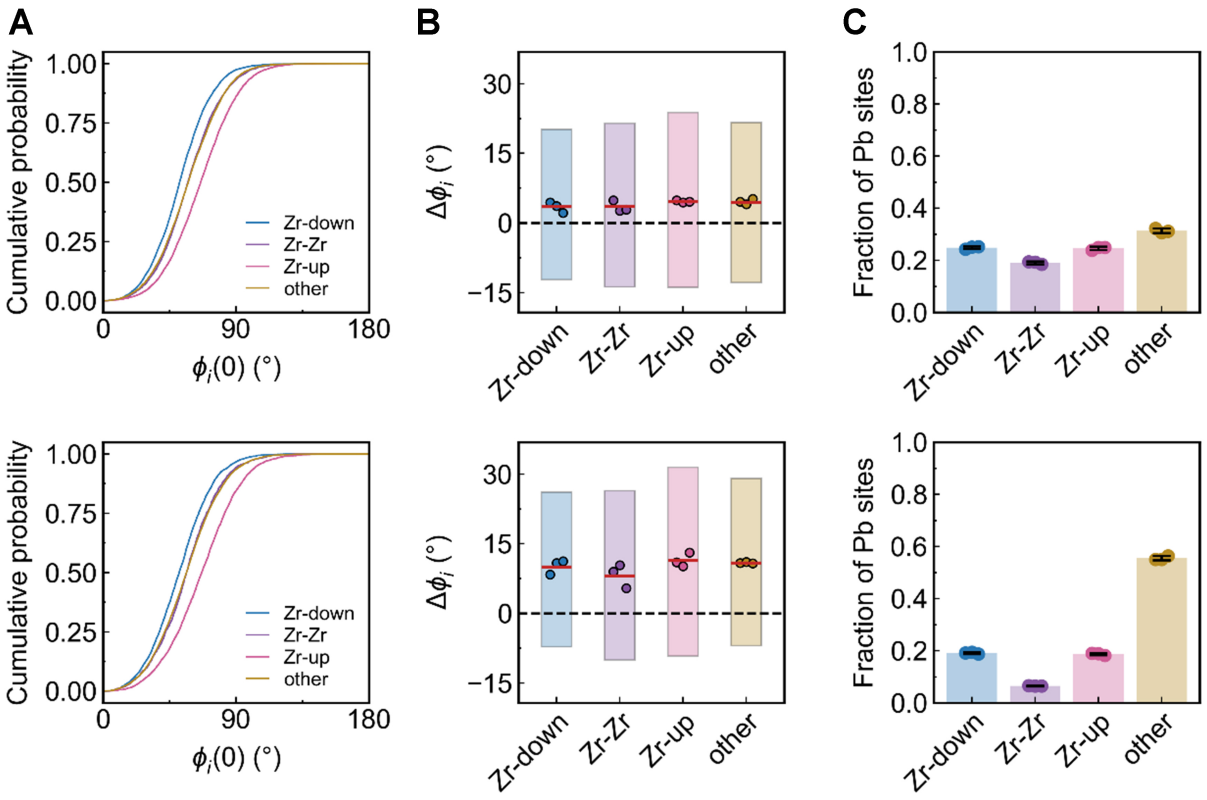


Figure 10. Local chemical dependence of Pb-displacement orientations and field-induced reorientation at 300 K. The upper and lower rows show results for x = 0.42 and x = 0.54, respectively. (A) Cumulative distributions of the zero-field deviation angle $\phi(0)$ between the local Pb off-center displacement and $[001]_p$, resolved into Zr-down, Zr-Zr, Zr-up and other-environments as defined in the text; (B) Site-resolved angular changes, $\Delta\phi = \phi(0) - \phi(100)$, upon increasing the electric field from 0 to 100 kV/cm along $[001]_p$. Positive values indicate rotation towards the field direction. Shaded boxes span the 25th-75th percentiles, red horizontal lines indicate medians, and circles show the median values from three independent simulation replicas. Dashed horizontal lines mark $\Delta\phi = 0$; (C) Fractions of Pb sites belonging to each local-environment category. Bars show the mean fractions across three independent simulation replicas, circles indicate the values for individual replicas, and black error bars represent the standard deviation. Angular quantities are calculated from the final equilibrated frame at each field strength, retaining the same Pb sites selected by the zero-field criterion ($|\mathbf{u}(0)| \geq 0.2$ Å).

Before comparing environment-resolved angular responses, we examine their dependence on the initial Pb-displacement magnitude at 200, 300 and 400 K [Supplementary Figures 16-18]. Sites with $|\mathbf{u}(0)| < 0.2$ Å generally exhibit broader angular-response distributions. For such small displacement vectors, a small change in the vector can produce a substantial change in its direction. We therefore restrict the following angular analysis to sites with $|\mathbf{u}(0)| \geq 0.2$ Å, applying this criterion only at zero field and following the same sites at 100 kV/cm. This excludes approximately 1.6%-2.2% of Pb sites at 300 K.

The deviation angle ϕ, measured between the local Pb off-center displacement and $[001]_p$, shows a pronounced dependence on the local chemical environment at zero field [Figure 10A]. At 300 K, distributions in Zr-down environments are shifted towards smaller angles, whereas those in Zr-up environments are shifted towards larger angles. Zr-Zr environments and other-environments exhibit intermediate distributions. Thus, the position of the Zr-rich plane relative to Pb is associated with a distinct initial orientational bias. At 100 kV/cm, Zr-down environments generally remain more closely aligned with the field than Zr-up environments, while the distributions for x = 0.54 shift towards smaller angles relative to those for x = 0.42 [Supplementary Figure 19].

To distinguish the initial orientational bias and final alignment from the magnitude of field-induced reorientation, we calculate the site-resolved angular change, $\Delta\phi = \phi(0) - \phi(100)$, where the field strengths are expressed in kV/cm. Positive values indicate rotation towards the field direction. The median $\Delta\phi$ values are larger for $x = 0.54$ across all four environment categories [Figure 10B], showing that the compositional contrast persists within the same local-environment classification. Within $x = 0.54$, Zr-up environments exhibit the largest median angular reduction, whereas Zr-Zr environments exhibit the smallest. The larger angular reduction in Zr-up environments coexists with their larger initial deviation angles and does not imply that they achieve the closest final alignment or possess the lowest rotational barriers. The smaller median response of Zr-Zr environments is consistent with more restricted field-induced reorientation between two Zr-rich planes. The interquartile ranges span both positive and negative $\Delta\phi$, revealing substantial site-to-site variation despite the positive median responses. Results at 200 and 400 K likewise show larger median angular changes for $x = 0.54$ across all four environment categories [Supplementary Figures 20 and 21].

The composition-dependent fractions of these local environments provide a further connection between local chemistry and the collective response [Figure 10C]. Zr-up and Zr-down environments have similar fractions within each composition, and both fractions decrease modestly from ($x = 0.42$) to ($x = 0.54$). Meanwhile, the Zr-Zr fraction decreases substantially, whereas other-environments become more abundant and constitute the dominant population at ($x = 0.54$). The MPB composition therefore combines a reduced population of environments bounded by two Zr-rich planes with larger angular responses within each environment category. Together, these results suggest that local chemical environments contribute to both the orientational diversity and the field-induced reorientability of Pb displacements, supporting the enhanced polarization rotation and electromechanical response near the MPB.

CONCLUSIONS

Using the newly developed NEP for PZT, we resolve the evolution of collective octahedral ordering and local rotational dynamics upon cooling in Zr-rich PZT. Local rotations are already present at high temperatures, where they fluctuate among several symmetry-equivalent directions. Cooling first produces collective selection of an antiphase tilt axis and then progressively suppresses local rotational hopping, predominantly between neighboring $<111>_p$ directions separated by approximately 71°, eventually leading to effective dynamic freezing on the molecular-dynamics timescale. These results reveal a dynamical crossover in which collective antiphase tilt order coexists with local rotational hopping before the latter becomes largely suppressed. The associated characteristic temperatures describe changes in rotational dynamics and should not be directly identified with the experimental R3m–R3c phase boundary.

Near the MPB, applied electric fields drive polarization rotation through the reorientation of Pb off-center displacements, with the collective orientational redistribution consistent with $R \rightarrow M_A \rightarrow T$. The enhanced strain response is not determined by the abundance of these monoclinic-like intermediate configurations alone, but by the extent to which Pb displacements can reorient under the applied field. Comparing the Zr-rich and MPB compositions shows that local Zr/Ti environments bias the initial Pb-displacement orientations and modulate their angular responses. Near the MPB, a smaller fraction of Zr-Zr environments coexists with larger field-induced angular changes within all four environment categories. These results support a picture in which local chemical environments contribute to the enhanced electromechanical response by modulating the orientational preferences and field-induced reorientation of Pb displacements.

These findings provide atomistic interpretations of two distinct phenomena in PZT that cannot be obtained from the average phase diagram alone: the dynamic freezing of local octahedral rotations within the Zr-rich rhombohedral region and the chemically modulated reorientation of Pb displacements near the MPB. They

further highlight the importance of resolving the temporal evolution and field response of local structural motifs for understanding the composition-dependent phase behavior and electromechanical response of chemically disordered ferroelectric solid solutions.

DECLARATIONS

Authors' contributions

Conceived the project and designed the research strategy: Huang, X.; Zhan, H.
Performed the first-principles density functional theory calculations and constructed the machine learning potentials: Huang, X.
Conducted the large-scale molecular dynamics simulations and executed the phase transition and polarization rotation analyses: Huang, X.; Nie, Y.; Zhan, H.
Developed the analytical codes and visualization protocols: Huang, X.
Interpreted the physical mechanisms and thermodynamic data: Huang, X.; Nie, Y.; Zhan, H.; Zhang, G.; Lü, C.
Wrote the initial draft of the manuscript: Huang, X.
All authors contributed to the critical discussion, revision, and approval of the final version of the manuscript.

Availability of data and materials

The datasets generated and analyzed during the current study, including the first-principles training dataset, trained neuroevolution potential (NEP) files, and analyzed structural trajectories, are openly available in the GitHub repository: https://github.com/ZJUNanotech/Neuroevolution-Potential.git.

AI and AI-assisted tools statement

During the preparation of this manuscript, the authors used ChatGPT (OpenAI) to assist with language editing, grammar correction, and improving the readability of the manuscript. No AI tools were used to generate or modify any figures, graphical abstracts, or schematic illustrations. The AI tool did not influence the study design, data collection, analysis, interpretation, or the scientific content of the work. All authors reviewed and edited the AI-assisted text and take full responsibility for the accuracy, integrity, and final content of the manuscript.

Financial support and sponsorship

Lü, C. would like to thank the financial support from the National Natural Science Foundation of China (Grant No. U22A20254); Zhan, H. would like to thank the financial support from the Zhejiang Provincial Natural Science Foundation of China (Grant No. LRG26A020002) and the National Natural Science Foundation of China (Grant No. 12572129); Nie, Y. would like to thank the financial support from the Zhejiang Provincial Natural Science Foundation of China (Grant No. LMS26A020001).

Conflicts of interest

Zhang, G. is an Advisory Editor of the journal *Journal of Materials Informatics*, but was not involved in any steps of editorial processing, notably including reviewer selection, manuscript handling, and decision-making, while the other authors have declared that they have no conflicts of interest.

Ethical approval and consent to participate

Not applicable.

Consent for publication

Not applicable.

Copyright

© The Author(s) 2026.

Supplementary Materials

Supplementary Materials

REFERENCES

1. Pan, X.; Wu, Y.; Wang, Y.; Zhou, G.; Cai, H. Mechanical energy harvesting based on the piezoelectric materials: recent advances and future perspectives. *Chem. Eng. J.* **2024**, *497*, 154249. DOI
2. Pang, F.; Zhao, P.; Lee, H. Y.; et al. Progress and perspectives in 2D piezoelectric materials for piezotronics and piezo-phototronics. *Adv. Sci.* **2025**, *12*, e2411422. DOI PubMed PMC
3. Niu, J.; Wei, Y.; Deng, Y.; et al. Record high-temperature piezoelectric performance in BNKT-based single crystals via local heterostructure design. *J. Mater. Scie. Technol.* **2026**, *271*, 147-56. DOI
4. Safaltin, S.; Nayak, S. K.; Alpay, S. Tailoring dielectric, piezoelectric and ferroelectric properties in aluminum scandium nitride through doping. *Acta. Mater.* **2026**, *308*, 122040. DOI
5. Kroutvar, M.; Ducommun, Y.; Heiss, D.; et al. Optically programmable electron spin memory using semiconductor quantum dots. *Nature* **2004**, *432*, 81-4. DOI PubMed
6. Bell, A. J.; Deubzer, O. Lead-free piezoelectrics - the environmental and regulatory issues. *MRS. Bull.* **2018**, *43*, 581-7. DOI
7. Fan, W.; Lei, R.; Dou, H.; et al. Sweat permeable and ultrahigh strength 3D PVDF piezoelectric nanoyarn fabric strain sensor. *Nat. Commun.* **2024**, *15*, 3509. DOI PubMed PMC
8. Yang, Z.; Yuan, M.; Liu, B.; et al. Dual-defect regulated G-C_3N_4 for piezoelectric catalytic tumor therapy with enhanced efficacy. *Adv. Mater.* **2025**, *37*, e2412069. DOI PubMed
9. Li, J.; Qu, W.; Daniels, J.; et al. Lead zirconate titanate ceramics with aligned crystallite grains. *Science* **2023**, *380*, 87-93. DOI PubMed
10. Liu, C.; Du, Q.; Wu, J.; Zhang, G.; Shi, Y. Novel 3D printed PZT-based piezoceramics for piezoelectric energy harvesting via digital light processing. *Chem. Eng. J.* **2024**, *492*, 152004. DOI
11. Tang, M.; Liu, X.; Zheng, S.; et al. Electric field control of piezoelectricity in textured PMN-PZT ceramics. *J. Mater. Sci. Technol.* **2025**, *224*, 10-8. DOI
12. Su, Y.; Han, T.; Xu, L.; et al. Concurrent optimization of d_{33} and Q_m in PZT-based ceramics via defect and phase-boundary engineering. *J. Am. Ceram. Soc.* **2026**, *109*, e70651. DOI
13. Jaffe, B.; Cook, W. R.; Jaffe, H. Chapter 6 - Properties of $PbTiO_3$, $PbZrO_3$, $PbSnO_3$, and $PbHfO_3$ plain and modified. In *Piezoelectric ceramics*. Elsevier; 1971. pp. 115-34. DOI
14. Noheda, B.; Cox, D. E.; Shirane, G.; Gonzalo, J. A.; Cross, L. E.; Park, S. E. A monoclinic ferroelectric phase in the $Pb(Zr_{1-x}Ti_x)O_3$ solid solution. *Appl. Phys. Lett.* **1999**, *74*, 2059-61. DOI
15. Noheda, B.; Cox, D. E.; Shirane, G.; Guo, R.; Jones, B.; Cross, L. E. Stability of the monoclinic phase in the ferroelectric perovskite $PbZr_{1-x}Ti_xO_3$. *Phys. Rev. B.* **2000**, *63*, 014103. DOI
16. Noheda, B.; Gonzalo, J. A.; Caballero, A. C.; Moure, C.; Cox, D. E.; Shirane, G. New features of the morphotropic phase boundary in the $Pb(Zr_{1-x}Ti_x)O_3$ system. *Ferroelectrics* **2000**, *237*, 237-44. DOI
17. Bellaiche, L.; Garcia, A.; Vanderbilt, D. Finite-temperature properties of $Pb(Zr_{1-x}Ti_x)O_3$ alloys from first principles. *Phys. Rev. Lett.* **2000**, *84*, 5427-30. DOI PubMed
18. Guo, R.; Cross, L. E.; Park, S. E.; Noheda, B.; Cox, D. E.; Shirane, G. Origin of the high piezoelectric response in $PbZr_{1-x}Ti_xO_3$. *Phys. Rev. Lett.* **2000**, *84*, 5423-6. DOI PubMed
19. Vanderbilt, D.; Cohen, M. H. Monoclinic and triclinic phases in higher-order Devonshire theory. *Phys. Rev. B.* **2001**, *63*, 094108. DOI
20. Wu, Z.; Krakauer, H. First-principles calculations of piezoelectricity and polarization rotation in $Pb(Zr_{0.5}Ti_{0.5})O_3$. *Phys. Rev. B.* **2003**, *68*, 014112. DOI
21. Fu, H.; Cohen, R. E. Polarization rotation mechanism for ultrahigh electromechanical response in single-crystal piezoelectrics. *Nature* **2000**, *403*, 281-3. DOI PubMed
22. Damjanovic, D. Contributions to the piezoelectric effect in ferroelectric single crystals and ceramics. *J. Am. Ceram. Soc.* **2005**, *88*, 2663-76. DOI
23. Zhang, N.; Yokota, H.; Glazer, A. M.; et al. The missing boundary in the phase diagram of $PbZr_{1-x}Ti_xO_3$. *Nat. Commun.* **2014**, *5*, 5231. DOI PubMed
24. Liu, H.; Chen, J.; Fan, L.; et al. Critical role of monoclinic polarization rotation in high-performance perovskite piezoelectric materials. *Phys. Rev. Lett.* **2017**, *119*, 017601. DOI
25. Niu, J.; Li, C.; Xi, Z. The intrinsic piezoelectricity of monoclinic $Pb(Zr_{1-x}Ti_x)O_3$. *RSC. Adv.* **2024**, *14*, 38245-52. DOI PubMed PMC
26. Dmowski, W.; Egami, T.; Farber, L.; Davies, P. K. Structure of $Pb(Zr, Ti)O_3$ near the morphotropic phase boundary. *AIP. Conf. Proc.* **2001**, *582*, 33-44. DOI

27. Grinberg, I.; Cooper, V. R.; Rappe, A. M. Relationship between local structure and phase transitions of a disordered solid solution. *Nature* **2002**, *419*, 909-11. DOI PubMed
28. Randall, C. A.; Matsko, M. G.; Cao, W.; Bhalla, A. S. A transmission electron microscopy investigation of the R3m → R3c phase transition in Pb(Zr,Ti)O_3 ceramics. *Solid. State. Commun.* **1993**, *85*, 193-5. DOI
29. Viehland, D.; Li, J.; Dai, X.; Xu, Z. Structural and property studies of high Zr-content lead zirconate titanate. *J. Phys. Chem. Solids.* **1996**, *57*, 1545-54. DOI
30. Cordero, F.; Trequattrini, F.; Craciun, F.; Galassi, C. Octahedral tilting, monoclinic phase and the phase diagram of PZT. *J. Phys. Condens. Matter.* **2011**, *23*, 415901. DOI PubMed
31. Zhang, N.; Yokota, H.; Glazer, A. M.; Thomas, P. A. The *not so* simple cubic structure of $PbZr_{1-x}Ti_xO_3$ (PZT): complex local structural effects in perovskites. *Acta. Crystallogr. B.* **2011**, *67*, 461-6. DOI PubMed
32. Shi, Y.; He, R.; Zhang, B.; Zhong, Z. Revisiting the phase diagram and piezoelectricity of lead zirconate titanate from first principles. *Phys. Rev. B.* **2024**, *109*, 174104. DOI
33. Sepliarsky, M.; Asthagiri, A.; Phillpot, S.; Stachiotti, M.; Migoni, R. Atomic-level simulation of ferroelectricity in oxide materials. *Curr. Opin. Solid. State. Mater. Sci.* **2005**, *9*, 107-13. DOI
34. Shin, Y. H.; Cooper, V. R.; Grinberg, I.; Rappe, A. M. Development of a bond-valence molecular-dynamics model for complex oxides. *Phys. Rev. B.* **2005**, *71*, 054104. DOI
35. Kitamura, T.; Umeno, Y.; Shang, F.; Shimada, T.; Wakahara, K. Development of interatomic potential for Pb(Zr, Ti)O_3 based on shell model. *J. Solid. Mech. Mater. Eng.* **2007**, *1*, 1423-31. DOI
36. Shimada, T.; Wakahara, K.; Umeno, Y.; Kitamura, T. Shell model potential for $PbTiO_3$ and its applicability to surfaces and domain walls. *J. Phys. Condens. Matter.* **2008**, *20*, 325225. DOI
37. Gindele, O.; Kimmel, A.; Cain, M. G.; Duffy, D. Shell model force field for lead zirconate titanate $Pb(Zr_{1-x}Ti_x)O_3$. *J. Phys. Chem. C.* **2015**, *119*, 17784-9. DOI
38. Thong, H. C.; Wang, X. Y.; Han, J.; et al. Machine learning interatomic potential for molecular dynamics simulation of the ferroelectric $KNbO_3$ perovskite. *Phys. Rev. B.* **2023**, *107*, 014101. DOI
39. Wu, J.; Yang, J.; Liu, Y. J.; et al. Universal interatomic potential for perovskite oxides. *Phys. Rev. B.* **2023**, *108*, L180104. DOI
40. Zhang, H.; Thong, H. C.; Bastogne, L.; Gui, C.; He, X.; Ghosez, P. Finite-temperature properties of the antiferroelectric perovskite $PbZrO_3$ from a deep-learning interatomic potential. *Phys. Rev. B.* **2024**, *110*, 054109. DOI
41. Zhang, J.; Zhang, H.; Zheng, H.; Xu, B.; Wang, J.; Guo, X. On-the-fly machine learning-assisted high accuracy second-principles model for $BaTiO_3$. *npj. Comput. Mater.* **2025**, *11*, 1787. DOI
42. Zhang, X.; Li, B.; Wang, M.; et al. Deep-learning potential with anisotropic effective charge tensors for ab initio ferro-piezoelectricity of lead-free (K, Na)NbO_3 perovskites. *Ceram. Int.* **2025**, *51*, 47675-84. DOI
43. Fan, Z.; Zeng, Z.; Zhang, C.; et al. Neuroevolution machine learning potentials: combining high accuracy and low cost in atomistic simulations and application to heat transport. *Phys. Rev. B.* **2021**, *104*, 104309. DOI
44. Song, K.; Zhao, R.; Liu, J.; et al. General-purpose machine-learned potential for 16 elemental metals and their alloys. *Nat. Commun.* **2024**, *15*, 10208. DOI PubMed PMC
45. Kresse, G.; Furthmüller, J. Efficient iterative schemes for ab initio total-energy calculations using a plane-wave basis set. *Phys. Rev. B. Condens. Matter.* **1996**, *54*, 11169-86. DOI PubMed
46. Kresse, G.; Joubert, D. From ultrasoft pseudopotentials to the projector augmented-wave method. *Phys. Rev. B.* **1999**, *59*, 1758-75. DOI
47. Perdew, J. P.; Ruzsinszky, A.; Csonka, G. I.; et al. Restoring the density-gradient expansion for exchange in solids and surfaces. *Phys. Rev. Lett.* **2008**, *100*, 136406. DOI
48. Togo, A. First-principles phonon calculations with Phonopy and Phono3py. *J. Phys. Soc. Jpn.* **2023**, *92*, 012001. DOI
49. Plimpton, S. Fast parallel algorithms for short-range molecular dynamics. *J. Comput. Phys.* **1995**, *117*, 1-19. DOI
50. Momma, K.; Izumi, F. *VESTA 3* for three-dimensional visualization of crystal, volumetric and morphology data. *J. Appl. Crystallogr.* **2011**, *44*, 1272-6. DOI
51. van de Walle, A.; Tiwary, P.; de Jong, M.; et al. Efficient stochastic generation of special quasirandom structures. *Calphad* **2013**, *42*, 13-8. DOI
52. Zhong, W.; King-Smith, R. D.; Vanderbilt, D. Giant LO-TO splittings in perovskite ferroelectrics. *Phys. Rev. Lett.* **1994**, *72*, 3618-21. DOI PubMed
53. Kabsch, W. A solution for the best rotation to relate two sets of vectors. *Acta. Cryst. A.* **1976**, *32*, 922-3. DOI
54. Gerber, P.; Böttger, U.; Waser, R. Composition influences on the electrical and electromechanical properties of lead zirconate titanate thin films. *J. Appl. Phys.* **2006**, *100*, 124105. DOI

55. Morioka, H.; Yokoyama, S.; Oikawa, T.; Funakubo, H.; Saito, K. Spontaneous polarization change with Zr/(Zr+Ti) ratios in perfectly polar-axis-orientated epitaxial tetragonal $Pb(Zr,Ti)O_3$ films. *Appl. Phys. Lett.* **2004**, *85*, 3516-8. DOI
56. Eggestad, K.; Skogvoll, I. C.; Gullbrekken, Ø.; Williamson, B. A. D.; Selbach, S. M. Finite-temperature ferroelectric phase transitions from machine-learned force fields. *Phys. Rev. Mater.* **2026**, *10*, 034409. DOI
57. Li, D.; Ahart, C. S.; Liu, S. Disentangling the discrepancy between theoretical and experimental Curie temperatures in ferroelectric $PbTiO_3$. *MRS. Commun.* **2026**, *16*, 1439-47. DOI
58. Paul, A.; Sun, J.; Perdew, J. P.; Waghmare, U. V. Accuracy of first-principles interatomic interactions and predictions of ferroelectric phase transitions in perovskite oxides: energy functional and effective Hamiltonian. *Phys. Rev. B.* **2017**, *95*, 054111. DOI
59. Gigli, L.; Goscinski, A.; Ceriotti, M.; Tribello, G. A. Modeling the ferroelectric phase transition in barium titanate with DFT accuracy and converged sampling. *Phys. Rev. B.* **2024**, *110*, 024101. DOI
60. Fan, Z.; Tang, B.; Berger, E.; et al. qNEP: a highly efficient neuroevolution potential with dynamic charges for large-scale atomistic simulations. *J. Chem. Theory. Comput.* **2026**, *22*, 4787-801. DOI

Disclaimer/Publisher's Note: All statements, opinions, and data contained in this publication are solely those of the individual author(s) and contributor(s) and do not necessarily reflect those of OAE and/or the editor(s). OAE and/or the editor(s) disclaim any responsibility for harm to persons or property resulting from the use of any ideas, methods, instructions, or products mentioned in the content.


© The Author(s) 2026. Open Access This article is licensed under a Creative Commons Attribution 4.0 International License (https://creativecommons.org/licenses/by/4.0/), which permits unrestricted use, sharing, adaptation, distribution and reproduction in any medium or format, for any purpose, even commercially, as long as you give appropriate credit to the original author(s) and the source, provide a link to the Creative Commons license, and indicate if changes were made.